Experimental and numerical analysis of Tm^{2+} excited-states dynamics and luminescence in CaX_2 (X = Cl, Br, I)

Plokker, M. P.; van der Knijff, I. C.; de Wit, A. V.; Voet, B.; Woudstra, T.; Khanin, V.; Dorenbos, P.; van der Kolk, E.

DOI
10.1088/1361-648X/abfa5d

Publication date
2021

Document Version
Final published version

Published in
Journal of Physics Condensed Matter

Citation (APA)
Plokker, M. P., van der Knijff, I. C., de Wit, A. V., Voet, B., Woudstra, T., Khanin, V., Dorenbos, P., & van der Kolk, E. (2021). Experimental and numerical analysis of Tm^{2+} excited-states dynamics and luminescence in CaX_2 (X = Cl, Br, I). *Journal of Physics Condensed Matter*, *33*(25), Article 255701. https://doi.org/10.1088/1361-648X/abfa5d

Journal of Physics: Condensed Matter

Experimental and numerical analysis of Tm^{2+} excited-states dynamics and luminescence in CaX_2 (X = Cl, Br, I)

To cite this article: M P Plokker *et al* 2021 *J. Phys.: Condens. Matter* **33** 255701

OPEN ACCESS
IOP Publishing
Journal of Physics: Condensed Matter
J. Phys.: Condens. Matter **33** (2021) 255701 (12pp)
https://doi.org/10.1088/1361-648X/abfa5d

Experimental and numerical analysis of Tm^{2+} excited-states dynamics and luminescence in CaX_2 (X = Cl, Br, I)

M P Plokker[*], **I C van der Knijff, A V de Wit, B Voet, T Woudstra, V Khanin, P Dorenbos and E van der Kolk**

Luminescence Materials Research Group, Delft University of Technology, Mekelweg 15, 2629 JB Delft, The Netherlands

E-mail: m.p.plokker@tudelft.nl

Received 5 February 2021, revised 7 April 2021
Accepted for publication 21 April 2021
Published 21 May 2021

Abstract

The prospect of using Tm^{2+}-doped halides for luminescence solar concentrators (LSCs) requires a thorough understanding of the temperature dependent Tm^{2+} excited states dynamics that determines the internal quantum efficiency (QE) and thereby the efficiency of the LSC. In this study we investigated the dynamics in CaX_2:Tm^{2+} (X = Cl, Br, I) by temperature- and time-resolved measurements. At 20 K up to four distinct Tm^{2+} emissions can be observed. Most of these emissions undergo quenching via multi-phonon relaxation below 100 K. At higher temperatures, only the lowest energy 5d–4f emission and the 4f–4f emission remain. Fitting a numerical rate equation model to the data shows that the subsequent quenching of the 5d–4f emission is likely to occur initially via multi-phonon relaxation, whereas at higher temperatures additional quenching via interband crossing becomes thermally activated. At room temperature only the 4f–4f emission remains and the related QE becomes close to 30%. Possible reasons for the quantum efficiency not reaching 100% are provided.

Keywords: Tm^{2+} excited states dynamics, photoluminescence, rate equations modelling, luminescence quenching, Tm^{2+} doped halides, $CaCl_2$:Tm^{2+} $CaBr_2$:Tm^{2+} CaI_2:Tm^{2+}

S Supplementary material for this article is available online

(Some figures may appear in colour only in the online journal)

1. Introduction

LSCs can become one of many building-integrated photovoltaic (BIPV) solutions that contribute to more sustainable buildings. LSCs make use of a special luminescent coating that absorbs sunlight and emits light of different energy towards solar cells mounted in the edges of a window. The window glass serves as a waveguide for the emitted light. Key material challenges for the LSC coating involve: a large sunlight absorption fraction that includes ultraviolet and visible light, a high internal luminescence QE and the absence of self-absorption losses caused by a direct re-absorption of the emitted light by the coating [1, 2]. Tm^{2+}-doped halides have been identified as potential LSC coating material. The broad 4f–5d absorption bands allow it to absorb up to 63% of the solar spectrum (AM 1.5) while no self-absorption losses can occur due to the energy difference between the 4f–5d absorption and the 4f–4f emission. Besides, the energy of this emission corresponds well with the bandgap of copper indium selenide (CIS) solar cells. Furthermore, an optimised coating based on Tm^{2+}-doped halides can appear colourless

---

[*] Author to whom any correspondence should be addressed.

Table 1. Summary of the analytical sample characterisations.

Sample	mol % TmI_2[a]	mol % Tm ICP-OES	Tm^{2+}/Tm^{3+} ratio[b]	mol % Tm^{2+}[c]	Crystal phase	$\hbar\omega_{max}$ cm^{-1}	Host-corrected absorption %[d]	QE % (300 K)[d]
$CaCl_2:Tm^{2+}$	2.0	1.6	0.5:0.5	0.8	*Pnnm*	270 [9]	45 ± 2[d]	25 ± 2[d]
$CaBr_2:Tm^{2+}$	2.0	1.5	0.8:0.2	1.2	*Pnnm*	160 [10]	53 ± 2[e]	27 ± 2[e]
$CaI_2:Tm^{2+}$	1.0	1.2	0.7:0.3	0.8	*P*-3*m*1	120 [11]	44 ± 2[f]	28 ± 2[f]

[a] Nominal doping.
[b] From K–M absorption spectra.
[c] Calculated from ICP-OES and K–M absorption spectra.
[d] $\lambda_{exc} = 645$ nm $\{(^3H_6,t_{2g})_{S=1/2}\}$
[e] $\lambda_{exc} = 665$ nm $\{(^3H_6,t_{2g})_{S=1/2}\}$
[f] $\lambda_{exc} = 760$ nm $\{(^3H_6,t_{2g})_{S=1/2}\}$

due to the broad absorption range over the entire visible light region [3].

However, not much is known about the QE of the 4f–4f emission after 4f–5d excitation. This parameter is directly proportional to the overall LSC efficiency and is mainly determined by the Tm^{2+} excited-states dynamics [1, 2]. Such dynamics has been studied intensely for $CsCaX_3:Tm^{2+}$ (X = Cl, Br, I) tri-halide systems [4–6], but only once for some di-halides [7]. No QE values were reported in these works. In our previous study on $NaX:Tm^{2+}$ (X = Cl, Br, I) mono-halides [8] we investigated the excited-states dynamics and measured the QE, but we were unable to provide a full quantitative description of important processes such as: the quenching mechanism related to the lowest energy 5d–4f emission, the presence of the 4f–4f emission at 20 K, and the efficient non-radiative 5d–4f ground state route. We have therefore decided to extend our Tm^{2+} excited-states dynamics study to $CaX_2:Tm^{2+}$ (X = Cl, Br, I), where the substitution of Tm^{2+} on Ca^{2+}-sites required no charge compensation, making use of temperature- and time-resolved experiments; and a more quantitative approach using a numerical rate equation analysis. First, the excitation bands and emissions are classified. Subsequently, a qualitative description of the excited-states dynamics is provided for all three materials, followed by a quantitative modelling on $CaBr_2:Tm^{2+}$ of time- and temperature-dependent 5d–4f and 4f–4f intensities and finally an overall discussion is provided focusing on the recorded QE-values.

2. Experimental section

2.1. Powder synthesis and preparation

The $CaCl_2:Tm^{2+}$, $CaBr_2:Tm^{2+}$ and $CaI_2:Tm^{2+}$ powder samples were respectively prepared by mixing $CaCl_2$, $CaBr_2$ and CaI_2 (Alfa Aeser, 99.99%) with 1.0–2.0 mol % TmI_2. The mixtures were ground into a homogeneous powder and inserted into quartz ampoules, which were then attached to a vacuum/inert gas system. After evacuation to 10^{-1} mbar and three succeeding purges with dry nitrogen, the ampoules were evacuated further to 10^{-3} mbar. Subsequently, the powders were heated using four Tecla burners. After 0.5–1 min the powders had completely molten and the heating was stopped. The solidified samples were removed from the ampoules and ground into a fine powder sample. All handlings were performed under strictly inert and dry conditions in a glovebox (MBraun, Garching, Germany).

2.2. Analytical characterisations

The Tm concentration in the samples was determined by means of inductively coupled plasma–optically enhanced spectroscopy (ICP-OES) measurements, using a Perkin Elmer Optima 4300DV spectrometer (Perkin Elmer, Waltham Massachusetts, USA). Diluted standards of Ca and Tm were used to constitute an intensity-concentration calibration line. The obtained values are reported in table 1. Differences with the nominal TmI_2 doping can largely be attributed to the accuracy of the used balance.

Diffuse reflectance spectra were recorded with a Bruker Vertex V80 spectrometer (Bruker, Karlsruhe, Germany), where the determined Kubelka–Munk (K–M) absorption was used to estimate the Tm^{2+}/Tm^{3+} ratio present in the samples. This ratio is derived from the integrated absorption bands of the Tm^{2+} $^2F_{7/2} \rightarrow {}^2F_{5/2}$ and the Tm^{3+} $^3H_6 \rightarrow {}^3H_5$ transitions, in combination with their relative absorption strengths in NaI, that respectively amount to 1 and 3.4. These latter values were determined from the integrated absorption band values of purely doped Tm^{2+} and Tm^{3+} NaI samples combined with their ICP-OES Tm concentrations. The K–M spectra of the samples are provided in figure 1 in the supplementary information (https://stacks.iop.org/JPCM/33/255701/mmedia) (SI) and the retrieved Tm^{2+}/Tm^{3+} ratios are listed in table 1.

The x-ray diffraction patterns of the powders were obtained with a Philips X'pert-Pro diffractometer (Philips, Eindhoven, The Netherlands) in Bragg–Bretano geometry using CuK_α radiation. The measurements took place at room temperature from 8° to 80° 2-theta with a 0.008° resolution. Figure 2 in the SI shows the diffractograms. The crystallographic structures imply that the Tm^{2+} dopant ions that occupy Ca^{2+} sites have a (distorted) octahedral coordination leading to a lower 5d-triplet t-state and upper 5d-doublet e-state that are further split due to the octahedral distortion. Throughout this work we will use the short hand notation $(^{2s+1}L_J,t_{2g})_s$ to assign the excited $4f^{12}5d^1$ levels, where $^{2s+1}L_J$ represents the state of $4f^{12}$, t_{2g} denotes that the 5d-electron is in a level and stemming from the t-triplet, and s denotes the total electron spin of the excited state.

Fluorescence quantum yield measurements were performed using an Edinburgh FLS980 spectrometer (Edinburgh

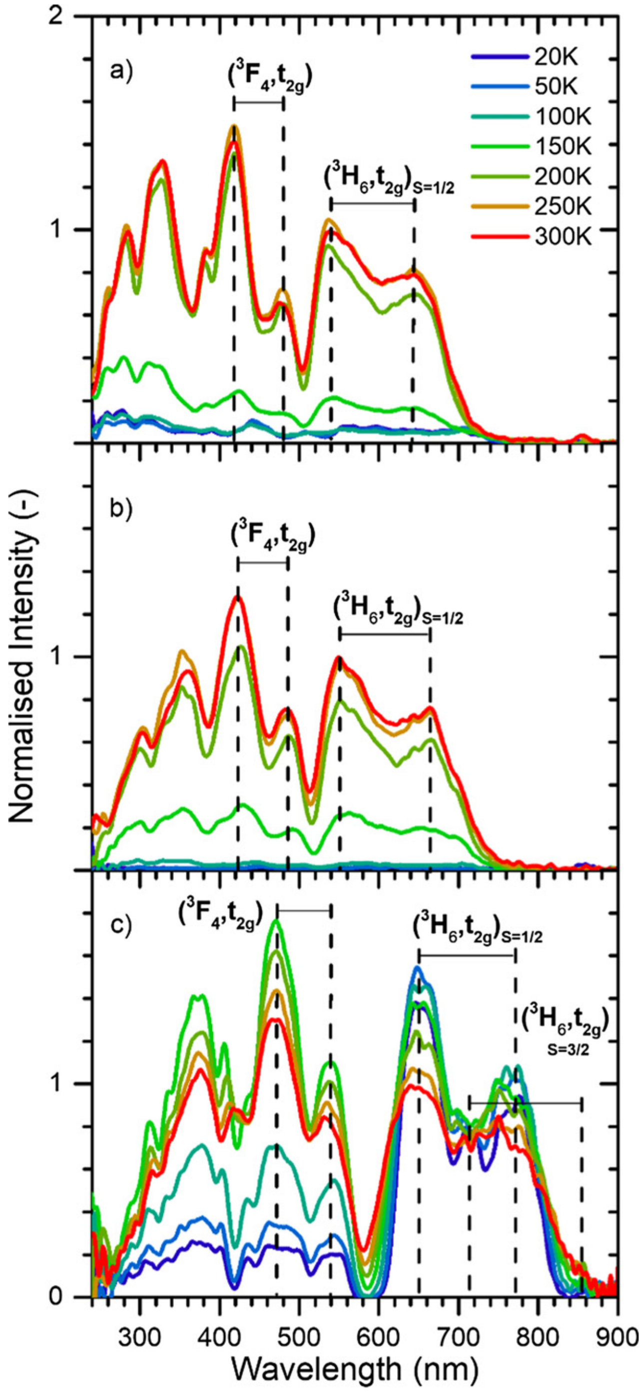

Figure 1. Normalised excitation spectra of: (a) $CaCl_2$:Tm^{2+}, (b) $CaBr_2$:Tm^{2+} and (c) CaI_2:Tm^{2+} as acquired on the Tm^{2+} $^2F_{5/2} \rightarrow {}^2F_{7/2}$ 4f–4f emission at 1140 nm and for different temperatures. The spectra are normalised on the LS $(^3H_6,t_{2g})_{S=1/2}$ band at 300 K.

Instruments, Livingston, UK) with an integrating sphere, a 450 W Xenon arc lamp and a Hamamatsu C9940-02 near infrared (NIR) photomultiplier tube (PMT) (Hamamatsu Photonics, Hamamatsu, Japan). The CaX_2:Tm^{2+} (X = Cl, Br, I) samples were excited into the Tm^{2+} $(^3H_6,t_{2g})_{S=1/2}$ level at room temperature and the reflectance was measured and compared to that of highly reflecting $BaSO_4$ and their undoped hosts. The absorption contributions of the CaX_2 (X = Cl, Br, I) hosts were respectively estimated at 4%, 2% and 4%.

From the amount of emitted and host-corrected absorbed photons, QE values were calculated and also added to table 1.

2.3. Temperature-dependent measurements

The temperature dependent emission and excitation spectra were obtained by using a xenon lamp coupled to a double monochromator with three gratings and a Hamamatsu C9100-13 EM-CCD or H1033A-75 NIR-PMT that was attached to a single monochromator with three gratings to record the luminescence emerging from the samples. A calibrated EPLAB NBS 1000W quartz iodine lamp was used to acquire the wavelength dependent sensitivity of the detectors. The detection ranges of 400:1150 nm and 950:1600 nm for CCD and NIR-PMT, respectively, share an overlap that allows it to couple the output of both detectors and hence accurately determine the 5d–4f and 4f–4f emission ratio's over temperature Since the Tm^{2+} $^2F_{7/2} \rightarrow {}^2F_{5/2}$ emission lies too close to the detection limit of the CCD detector, a small spatula amount of $Ca_2Si_5N_8$:Yb^{3+} was added to the samples. After exciting the Yb^{3+} at 360 nm, the $^2F_{5/2} \rightarrow {}^2F_{7/2}$ emission at 985 nm was observed and used for the detector coupling. With the applied Tm^{2+} excitation wavelengths ($(^3H_6,t_{2g})_{S=1/2}$-level), there is no overlap with any of the $Ca_2Si_5N_8$:Yb^{3+} excitation levels and hence only Tm^{2+} luminescence is observed [12].

Time resolved measurements were done with a tuneable EKSPLA NT230 laser (EKSPLA, Vilnius, Lithuania) that has a 7 ns pulse duration. DT5724F (0–2 ms) or DT5730 (0–40 ms) CAEN digitisers (CAEN, Viareggio, Italy) measured the signal from a H1033A-75 NIR-PMT or a Hamamatsu R7600U-20HV-800V PMT. The related decay curves were acquired by averaging over 1000 individual spectra.

The samples were heated and cooled with an APD Cryogenic Helium cooler (APD Cryogenics, Allentown Pennsylvania, USA) and Lakeshore temperature controller (Lakeshore Cryotronics, Westerville Ohio, USA).

Special hygroscopic sample holders protected the samples, during all measurements, against moisture and oxidation reactions. Similar sample holders were described by Rogers *et al* [13].

3. Results and discussion

3.1. Assignment of excitation bands

Figure 1 shows the excitation spectra of CaX_2:Tm^{2+} (X = Cl, Br, I) monitoring the Tm^{2+} $^2F_{5/2} \rightarrow {}^2F_{7/2}$ 4f–4f emission, at different temperatures. For $CaCl_2$:Tm^{2+} the spectra show much resemblance in shape to the earlier reported low temperature absorption spectra by Grimm *et al* [7] and Karbowiak *et al* [9]. Similarly, those of CaI_2:Tm^{2+} are akin to the room temperature absorption spectrum of Ten Kate *et al* [3]. The therein reported 5d-level classifications are appended to the spectra in figure 1.

The spectra display a clear separation of around 5700 cm^{-1} between the $(^3H_6,t_{2g})$ and $(^3F_4,t_{2g})$ levels, which follows from the 4f^{12}-level splitting into $^{2S+1}L_J$ terms that are analogous to the Tm^{3+} multiplets of the Dieke diagram [14]. In case of CaI$_2$:Tm^{2+}, an additional weak excitation band is observed close to 860 nm. Upon applying a redshift of 12 480 cm^{-1}, based on the works of Dorenbos [15], it follows that it represents a spin-forbidden (SF) transition to the (^{3}H$_6$,t$_{2g}$)$_{S=3/2}$ high-spin (HS) levels. For CaBr$_2$:Yb^{2+}, Larsen *et al* [16] observed the lowest energy low-spin (LS) and HS 5d-levels at respectively 25 133 and 23 696 cm^{-1}. Using retrieved redshifts of 10 797 and 10 304 cm^{-1}, respectively, these levels should then lie near 673 and 740 nm for CaBr$_2$:Tm^{2+}. The spectra in figure 1(b) indeed show a broad excitation band located at around 675 nm, thus representing the spin-allowed (SA) transition to the (^{3}H$_6$,t$_{2g}$)$_{S=1/2}$ LS levels. No band is observed near 740 nm in the excitation spectra of the 4f–4f emission. Instead the expected (^{3}H$_6$t$_{2g}$) HS band is well observed at low temperatures in the excitation spectra monitoring the HS 5d-emission itself, see figure 3 in the SI. As the excitation spectra of the 4f–4f transition only become intense at elevated temperatures, the HS band is likely hidden due to the broadening of the LS bands. This clearly seems to happen for CaI$_2$:Tm^{2+} and might also be the case for CaCl$_2$:Tm^{2+}.

3.2. Classification of emissions

In figure 2 the temperature dependent emission spectra of the three samples are displayed upon exciting into their (^{3}F$_4$,t$_{2g}$) levels. Up to four distinct Tm^{2+} emissions can be distinguished. These emissions are labelled R_{10} to R_{40} and their decay times and relative intensities are provided at 20 K or 300 K in table 2. For CaCl$_2$:Tm^{2+}, Grimm *et al* [7] already identified the emissions in accordance to their transition. Since the energy of the Stokes' shift is in first approximation the same for all lanthanides in a specific host, reported literature values from for instance CaBr$_2$:Eu^{2+} and CaI$_2$:Eu^{2+} can be added to our observed emissions in CaBr$_2$:Tm^{2+} and CaI$_2$:Tm^{2+} to establish a direct connection with the excitation bands in figure 1 and hence retrieve the transitions related to the emissions. Figure 3 serves as a schematic overview of all excitation bands and emissions.

In case of CaBr$_2$:Eu^{2+}, the Stokes' shift energy related to the SA 4f^6[^{7}F$_0$]5d^1 → 4f^7[^{8}S$_{7/2}$] transition amounts to 1232 cm^{-1} [16]. When adding this value to the observed 5d–4f emissions in CaBr$_2$:Tm^{2+} a good match is found with the excitation bands in figure 1(b). Emission R_{40} is found to stem from the (^{3}F$_4$,t$_{2g}$) band near 490 nm, relating it to the (^{3}F$_4$,t$_{2g}$) → ^{2}F$_{7/2}$ transition. It has a rather short decay time of 16 ns. Emission R_{20} corresponds to the HS (^{3}H$_6$,t$_{2g}$) level close to 740 nm, coupling it to the SF (^{3}H$_6$,t$_{2g}$)$_{S=3/2}$ → ^{2}F$_{7/2}$ transition.

Applying the Stokes' shift of 1885 cm^{-1} from CaI$_2$:Eu^{2+} [17, 18] onto CaI$_2$:Tm^{2+}, emission R_{30} can be coupled to the LS (^{3}H$_6$,t$_{2g}$) band at 770 nm and thus related to the (^{3}H$_6$,t$_{2g}$)$_{S=1/2}$ → ^{2}F$_{7/2}$ transition. Its SA nature is reflected in its order of magnitude shorter decay time compared to emission R_{20}. For CaCl$_2$:Tm^{2+} and CaBr$_2$:Tm^{2+}, emission R_{30} seems absent. The energy of emission R_{10} perfectly matches the ^{2}F5/2 → ^{2}F7/2 transition. Its strongly forbidden nature is reflected in a relatively long decay time of a few milliseconds.

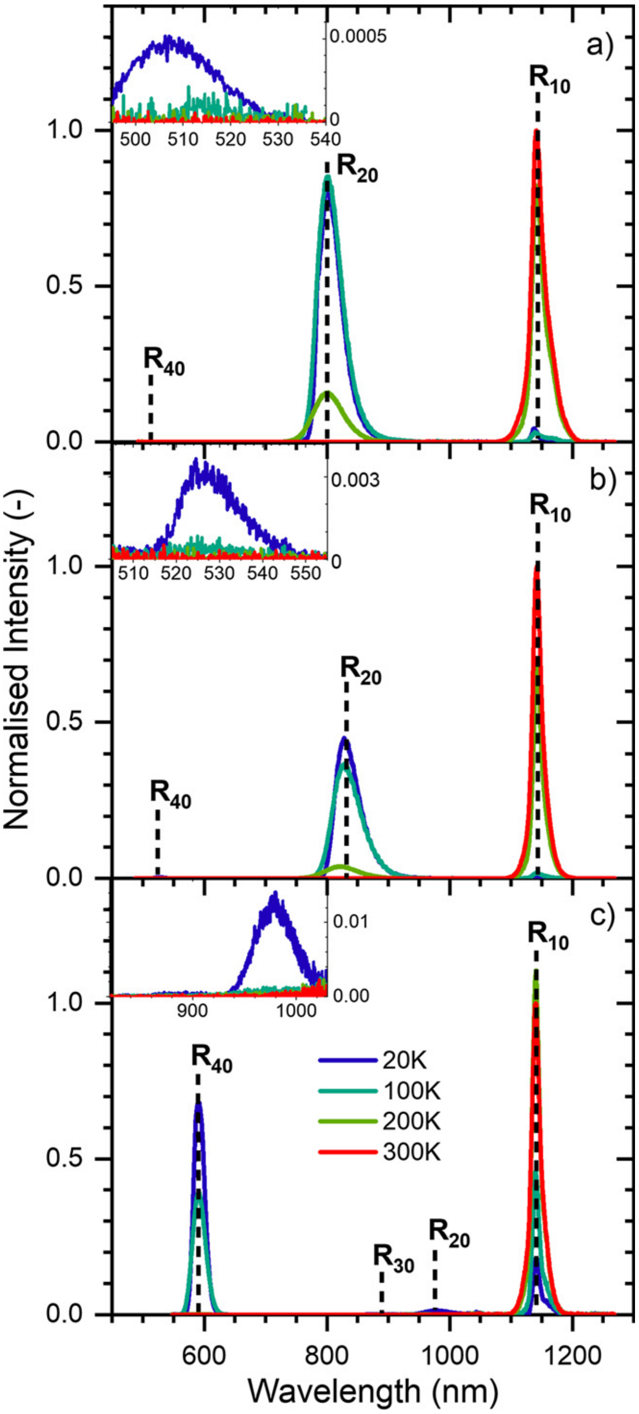

Figure 2. Normalised emission spectra of: (a) CaCl$_2$:Tm^{2+}, (b) CaBr$_2$:Tm^{2+} and (c) CaI$_2$:Tm^{2+} at different temperatures and normalised on the Tm^{2+} ^{2}F$_{5/2}$ → ^{2}F$_{7/2}$ emission at 300 K. Photoexcitation occurred within the (^{3}F$_4$,t$_{2g}$) levels at respectively 480 nm, 490 nm and 535 nm.

3.3. Qualitative description of temperature-dependent luminescence behaviour

The temperature dependent emission spectra of the materials reveal that, upon exciting into the (^{3}F$_4$,t$_{2g}$) band at 20 K,

Table 2. Summary overview of observed Tm^{2+} emissions in $CaX_2:Tm^{2+}$ (X = Cl, Br, I) after excitation into the $(^3F_4,t_{2g})$ levels.

Sample [-]	Emission [-]	Transition [-]	Wavelength (20 K) (nm)	Energy (20 K) (cm^{-1})	Decay time	Rel. integr. int. (20 K) [-]
$CaCl_2:Tm^{2+}$	R_{40}	$(^3F_4,t_{2g}) \rightarrow {}^2F_{7/2}$	508	19 685	9 ns (20 K)	1
	R_{20}	$(^3H_6,t_{2g})_{S=3/2} \rightarrow {}^2F_{7/2}$	801	12 484	350 μs (20 K)	3679
	R_{10}	$^2F_{5/2} \rightarrow {}^2F_{7/2}$	1138	8787	4.7 ms (300 K)	82
$CaBr_2:Tm^{2+}$	R_{40}	$(^3F_4,t_{2g}) \rightarrow {}^2F_{7/2}$	526	19 012	16 ns (20 K)	1
	R_{20}	$(^3H_6,t_{2g})_{S=3/2} \rightarrow {}^2F_{7/2}$	815	12 270	340 μs (20 k)	399
	R_{10}	$^2F_{5/2} \rightarrow {}^2F_{7/2}$	1139	8780	4.3 ms (300 K)	2
$CaI_2:Tm^{2+}$	R_{40}	$(^3F_4,t_{2g}) \rightarrow {}^2F_{7/2}$	596	16 779	1.5 μs (20 K)	933
	R_{30}	$(^3H_6,t_{2g})_{S=1/2} \rightarrow {}^2F_{7/2}$	883	11 325	1.6 μs (20 K)	1
	R_{20}	$(^3H_6,t_{2g})_{S=3/2} \rightarrow {}^2F_{7/2}$	978	10 225	36 μs (20 K)	37
	R_{10}	$^2F_{5/2} \rightarrow {}^2F_{7/2}$	1141	8764	3.6 ms (300 K)	193

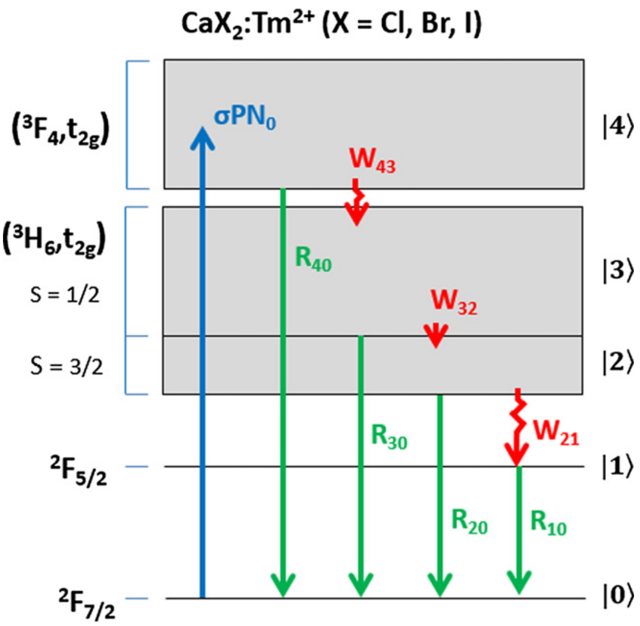

Figure 3. Schematic energy level diagram for $CaX_2:Tm^{2+}$ upon exciting into the $(^3F_4,t_{2g})$ levels (blue arrow). At 20 K up to four distinct Tm^{2+} emissions are be observed. These radiative transitions are indicated by the green straight arrows R_{ij}, while non-radiative quenching transitions W_{ij} are indicated by the red curly arrows. Here, index i refers to starting level and j the closing level.

all four Tm^{2+} emissions are present. For $CaCl_2:Tm^{2+}$ and $CaBr_2:Tm^{2+}$ emission R_{40} quenches at a very fast rate and is barely observed at 100 K. In case of $CaI_2:Tm^{2+}$ emission R_{40} survives longer and vanishes at 190 K. The energy gap between the lowest energy $(^3F_4,t_{2g})$ and highest energy $(^3H_6,t_{2g})$ LS levels in $CaX_2:Tm^{2+}$ (X = Cl, Br, I) respectively amounts to 2245, 2160 and 3310 cm^{-1} which comprises approximately 9, 14 and 28 vibrational quanta, see table 1 Assuming a small configurational offset between the two $4f^{12}5d^1(t_{2g})$-levels [19], the quenching W_{43} as illustrated in figure 3 most likely occurs via multi-phonon relaxation. The fast quenching of emission R_{40} leads to a feeding of the $(^3H_6,t_{2g})$ LS levels and in case of $CaI_2:Tm^{2+}$ the presence of emission R_{30}. With an energy gap of 1100 cm^{-1} (around 10 vibrational quanta) between the LS and HS levels, the emission will quench rapidly via multi-phonon relaxation W_{32}, as witnessed in the emission spectra at 100 K. For $CaCl_2:Tm^{2+}$ and $CaBr_2:Tm^{2+}$ no emission R_{30} is detected. This could be explained by a very rapid quenching via multi-phonon relaxation [18] or an LS → HS resonance energy transfer exciting a neighbouring Tm^{2+} ion to its $(^3H_6,t_{2g})$ HS levels [20], as described further in section 3.5. When subtracting the Stokes' shift energies for $CaBr_2:Eu^{2+}$ from the lowest energy LS excitation bands of $CaBr_2:Tm^{2+}$ it follows that the energy of the $(^3H_6,t_{2g})$ LS emission is close to the $(^3H_6,t_{2g})$ HS absorption. The same is true for $CaCl_2:Tm^{2+}$. Both scenarios lead to a feeding of the $(^3H_6,t_{2g})$ HS levels from which emission R_{20} occurs. For $CaCl_2:Tm^{2+}$ and $CaBr_2:Tm^{2+}$ this 5d–4f emission already has a strong presence at 20 K. It gradually becomes weaker as the temperature increases. The opposite behaviour is observed for 4f–4f emission R_{10} because of a non-radiative feeding process W_{21}. For both materials the 5d–4f emission has fully quenched at respectively 270 K and 260 K and only 4f–4f emission R_{10} remains. For $CaI_2:Tm^{2+}$, emission R_{20} quenches at a significantly lower temperature of 110 K. It implies that within the temperature range of 110–190 K, only 5d–4f emission R_{40} is present; the others already feeding the $^2F_{5/2}$ level and leading to 4f–4f emission R_{10}. This behaviour for $CaI_2:Tm^{2+}$ is especially noticeable upon comparing with the excitation spectra of $CaCl_2:Tm^{2+}$ and $CaBr_2:Tm^{2+}$ in figure 1. For these latter materials the relative intensity of the 5d-excitation bands when monitoring the $^2F5/2 \rightarrow {}^2F7/2$ emission, is the same for all temperatures. For $CaI_2:Tm^{2+}$ the higher energy 5d-bands have a much lower intensity (because these result in emission R_{40}) compared to the lower energy 5d-bands that do result in $^2F_{5/2} \rightarrow {}^2F_{7/2}$ emission. From 190 K onwards all 5d–4f emissions in $CaI_2:Tm^{2+}$ have quenched so that excitation into the different 5d-bands all result in 4f–4f emission. The 5d-bands are now dictated by the oscillator strength of the 4f–5d transitions, as is also observed in case of $CaCl_2:Tm^{2+}$ and $CaBr_2:Tm^{2+}$.

As the energy gap between the $(^3H_6,t_{2g})_{S=3/2}$ and $^2F_{5/2}$ levels for $CaCl_2:Tm^{2+}$, $CaBr_2:Tm^{2+}$ and $CaI_2:Tm^{2+}$ respectively amounts to 3700, 3500 and 1460 cm^{-1} or 14, 22 and 13 vibrational quanta, the quenching mechanism related to emission R_{20} can well be multi-phonon relaxation (MPR). However, since it involves a 5d–4f relaxation there is a large configurational offset and the optical phonon coupling strength, as defined by the Huang–Rhys factor, will be strong.

Table 3. List of inserted starting parameters and obtained values from the steady state (st.st.) and non-steady state (non.st.st.) fitting on CaBr$_2$:Tm^{2+}. R^2-values related to the accuracy of the fits are provided.

Param.	Start. val.	Non.st.st val.	St.st val.
σPN_0 (s^{-1})	1	—	—
R_{10} (s^{-1})	187	—	—
R_{20} (s^{-1})	2952	—	—
$\hbar\omega_{\max}$ (cm^{-1})	160	197	191
ΔE (cm^{-1})	3500	—	—
$W_\mathrm{p}(0)$ (s^{-1})	52.4	30.9	72.53
k (cm^{-1} . K^{-1})	0.695	—	—
S	2 . 10^9	1.20 . 10^9	1.97 . 10^9
ε (cm^{-1})	1694	1685	1785
R^2-value	—	0.9957	0.9991

The configurational offset could enable quenching via interband crossing (IC) or inter-configurational relaxation [3, 21]. This quenching mechanism involves the configurational cross-over-point between the (^{3}H$_6$,t$_{2g}$)$_{S=3/2}$ and ^{2}F$_{5/2}$ levels, that can be breached at certain temperatures when enough energy becomes available. In case of a large Stokes' shift, the crossing point is likely to be breached at a lower temperature [22]. In the next subsection, the two proposed quenching mechanisms of MPR and IC for emission R_{20} will be examined into more detail.

3.4. Quantitative description of temperature-dependent luminescence behaviour

Since the quenching mechanism of 5d–4f emission R_{20} remains unclear, we have decided to evaluate it by performing a luminescence rate equations analysis on CaBr$_2$:Tm^{2+} involving all radiative and temperature-dependent non-radiative transitions after excitation into the (^{3}H$_6$,t$_{2g}$) LS band. With LS emission R_{30} not observed in CaBr$_2$:Tm^{2+}, we initially neglect its influence and assume the excitation will automatically end up in the lowest energy (^{3}H$_6$,t$_{2g}$) HS levels. The scheme portrayed in figure 3 then allows us to describe the excited state population N_i (i = 1, 2) of the ^{2}F$_{5/2}$ and (^{3}H$_6$,t$_{2g}$)$_{S=3/2}$ levels, respectively, via the rate equations below.

$$\frac{\mathrm{d}N_2(t)}{\mathrm{d}t} = \sigma PN_0 - N_2(t)\left\{R_{20} - W_{21}\right\}$$

$$\frac{\mathrm{d}N_1(t)}{\mathrm{d}t} = N_2(t)\,W_{21} - N_1(t)\,R_{10}.$$

In this coupled set of equations, R_{20} and R_{10} represent the radiative transition rates in s^{-1}, W_{21} the non-radiative transition or quenching rate of emission R_{20} in s^{-1}, P portrays the laser power in cm^{-1} s^{-1}, σ the absorption cross section per wavelength of excitation energy in cm and N_0 the electron groundstate population, which is in good approximation considered to be unaffected by the excitation.

Following the scenario that emission R_{20} quenches via multi-phonon relaxation, the non-radiative rate W_{21} can be described according to the Reisfeld model [24–26] that is provided below.

$$W_{21}(T) = W_\mathrm{p}(0)\cdot\left\{1 - \mathrm{e}^{\frac{-\hbar\omega_{\max}}{kT}}\right\}^{-p}.$$

In this relation: $\hbar\omega_{\max}$ represents the maximum optical phonon energy in cm^{-1}, k the Boltzmann constant in cm^{-1} . K^{-1} and T the temperature in K. Furthermore, p embodies the number of phonons consumed during the relaxation: $p \cong \Delta E/\hbar\omega_{\max}$ where ΔE is the energy gap in cm^{-1}. $W_\mathrm{p}(0)$ is the multi-phonon decay rate at 0 K and is defined further via the following relation:

$$W_\mathrm{p}(0) = W_0(0)\cdot\mathrm{e}^{\frac{-\alpha\Delta E}{\hbar\omega_{\max}}} \quad \text{with} \ :\alpha = \ln\left(\frac{p}{g}\right) - 1.$$

Here, $W_0(0)$ is the decay rate at $\Delta E = 0$ cm^{-1} and $T = 0$ K, and g the dimensionless electron-phonon coupling strength (Huang Rhys factor).

By considering the option of interband crossing, the non-radiative rate W_{21} follows the relation below [27, 28], where s represents the frequency factor in s^{-1}, ε the activation energy of the quenching process in cm^{-1}, k the Boltzmann constant in cm^{-1} . K^{-1} and T the temperature in K.

$$W_{21}(T) = s\cdot\mathrm{e}^{\left(\frac{-\varepsilon}{kT}\right)}.$$

Especially at low temperatures the two expressions for the non-radiative rate W_{21} predict a different temperature dependence, which should allow us to draw conclusions on their contribution to the observed non-radiative relaxation.

3.4.1. Model setting. The fitting of our rate equation model and related quenching mechanisms to the temperature- and time-dependent intensity data, requires a set of starting values for the different parameters. The pump rate constant σPN_0 can be chosen arbitrary and is set at 1, where upon exciting into level $|3\rangle$ we assume a rapid quenching towards level $|2\rangle$ from which we monitor emission R_{20}. The radiative rates R_{10} and R_{20} were estimated based on the luminescence lifetime of the emissions at respectively 20 and 30 K, assuming no quenching takes place at these temperatures.

For CaX_2:Tm (X = Cl, Br, I) no direct values for the phonon energies $\hbar\omega_{\max}$ coupling to Tm^{2+} are reported in literature. We have therefore decided to estimate these values based on known studies that involve such hosts, see table 1 [9–11]. The values are close to those reported for LaY_3 (Y = Cl, Br) [24]. The energy gap ΔE between levels $|2\rangle$ and $|1\rangle$ was determined on 3500 cm^{-1} and the required amount of vibrational quanta p to bridge it is around 22. A reasonable starting value for the $W_0(0)$ parameter was estimated from literature to be 1 . 10^{14} s^{-1} [24, 25]. Since not much is known on the electron-phonon coupling strength g between 5d- and 4f-states, the rough starting value of 2 was used from the numerical modelling work of Grimm *et al* [6]. The parameters constitute an overall $W_\mathrm{p}(0)$ parameter of 18.7 s^{-1}. As an overall fitting strategy $\hbar\omega_{\max}$ and $W_\mathrm{p}(0)$ are fitted, while ΔE was kept fixed.

In the case of IC, the thermal activation energy ε was approximated at 1694 cm^{-1} and retrieved from an Arrhenius plot of the integrated luminescence intensity of R_{20}, see

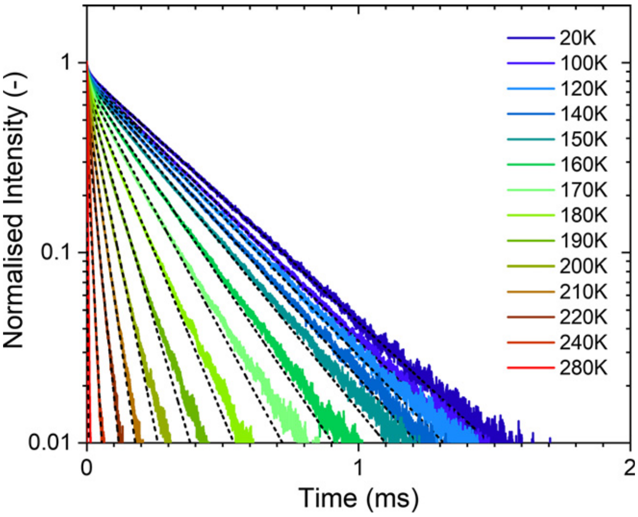

Figure 4. Normalised luminescence lifetime curves of 5d–4f emission R_{20} plotted at various temperatures. The dashed lines represent the single exponential fits based on our rate equations from which $W_{21}(T)$ values were obtained.

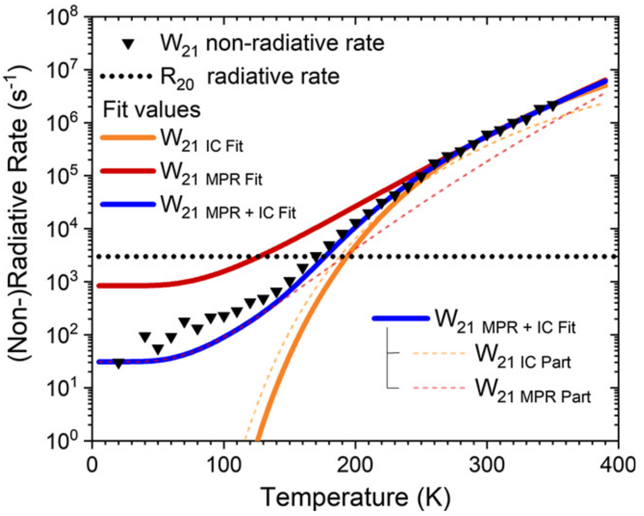

Figure 5. The obtained W_{21} values from figure 4plotted as black triangular points versus temperature. The fit based on purely MPR is shown in solid dark red, whereas that of IC is displayed in solid orange. The fit of the combined quenching (MPR + IC) is illustrated in blue with constituents MPR and IC respectively portrayed in dashed red and orange. The dotted black line shows the R_{20} radiative rate.

figure 4 in SI. From this Arrhenius plot the pre-exponential factor A was also determined and multiplied by R_{20} to obtain the frequency factor s of 1 . 10^9 s^{-1}. Both values are fitted to the data. All used starting values are listed in table 3.

3.4.2. Non-steady state rate equation analysis. The derived rate-equations can be solved in a non-steady-state manner, assuming a time-dependent depopulation of the levels, with solutions provided in section 7.5 of the SI. The solution for level $|2\rangle$ was fitted onto the measured luminescence lifetime curves of 5d–4f emission R_{20}. The related fits are displayed in figure 4, where from 300 K onwards the now weak emission is only faintly recorded. From each of the fit a value for W_{21} was obtained, allowing us to establish a $W_{21}(T)$ point series onto which the two quenching models can be tested.

Figure 5 shows this series as represented in black, where small error bars of 0.1%–5%, based on the fitting, are attached. The MPR model, shown in solid dark red, is able to reproduce the low-temperature trend among the W_{21} points. Yet, at high temperatures it is unable to mimic this and overall no accurate fit could be obtained. For IC, illustrated in solid orange, it is the other way around: an inaccurate representation at low temperature and a good depiction at high temperatures. Once more, the fit proved to be inaccurate. Based on these findings, the combined quenching via both MPR and IC was investigated. This option, as portrayed in blue, was able to provide a reasonable fit for both the low and high temperature range. The herewith obtained fitting parameters are added to table 3 and are close to our initial starting values; all within the same order of magnitude. For the combined quenching, the overall temperature development of MPR and IC are respectively portrayed in dashed red and dashed orange. The curves reveal that the low temperature regime is governed by MPR, whereas IC is dominant within the high temperature range. Furthermore, at around 170 K the non-radiative rate W_{21} becomes stronger than the radiative rate R_{20}, shown in dotted black, indicating that the quenching takes the upper hand.

3.4.3. Steady state rate equation analysis. The previously outlined set of coupled rate equations can also be solved in a steady state fashion, where a steady depopulation of the levels assumed. As elaborated in section 7.6 of the SI, the solutions combined with the radiative rates can be used for fitting luminescence intensity curves. Figure 6 shows such curves for emissions R_{20} and R_{10} in CaX_2:Tm^{2+} (X = Cl, Br, I) as a function of temperature, where the luminescence intensities of both emissions were corrected for the sensitivity of detection and coupled via the method described in section 2.3. The data was normalised on the measured QE values of emission R_{10} at room temperature, see table 1. For CaBr$_2$:Tm^{2+}, provided in panel b, the observed trends among the solid measured intensity data points are supported by those of the integrated luminescence lifetime curves from figure 4, displayed as open symbols. The light blue line shows a good fit for our combined quenching model (MPR + IC) onto the data points of emission R_{20}. The retrieved fitting parameters are appended to table 3 and are very close to both our original starting values and those obtained from the non-steady state fitting. When inserting these fitted parameter values in the rate equation solution for level N_1 (note that the fits were done on level N_2), the dotted red line is acquired which follows the overall data trend, but is shifted by 10 K towards lower temperature. Our fitted model predicts a lower temperature and intensity for the intersection point between the R_{20} and R_{10} curves. Furthermore, at 250 K the fitted model reaches an intensity plateau while for the experimental data it is reached at a higher temperature.

The similarity between the luminescence intensity curves of CaBr$_2$:Tm^{2+} and CaCl$_2$:Tm^{2+} has incited us to extend the

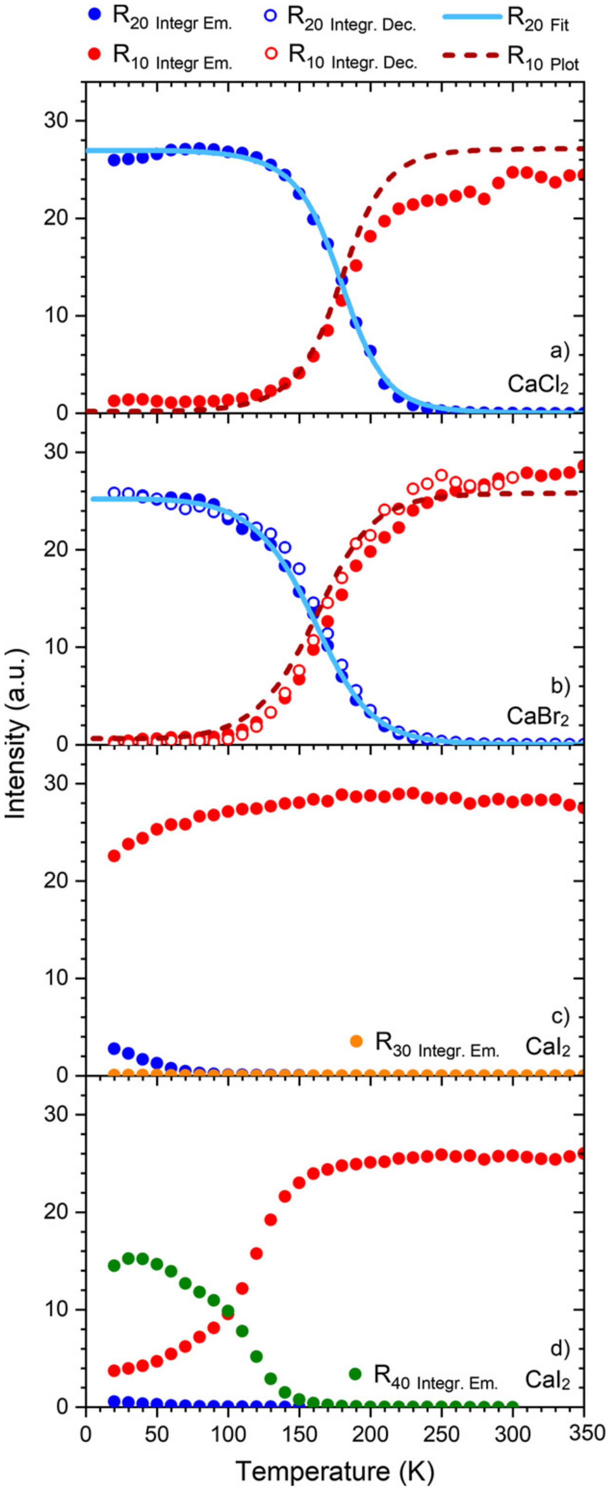

Figure 6. Plots of integrated emission intensity of 5d–4f emission R_{20} (solid blue) and 4f–4f emission R_{10} (solid red) versus temperature for: (a) $CaCl_2:Tm^{2+}$, (b) $CaBr_2:Tm^{2+}$ and (c) $CaI_2:Tm^{2+}$ upon excitation into ($^3H_6$,t_{2g}) LS levels. For $CaBr_2:Tm^{2+}$ the open symbols correspond to the integrated lifetime curves of emissions R_{20} and R_{10} revealing much equivalent trends. For $CaCl_2:Tm^{2+}$ and $CaBr_2:Tm^{2+}$, the light blue lines represent the steady state fits onto emission R_{20} with related plots of R_{10} displayed as dashed dark red lines. For $CaI_2:Tm^{2+}$ the data of emission R_{30} is portrayed in orange. Panel (d) shows similar data upon exciting into the ($^3F_4$,t_{2g}) levels with emission R_{40} displayed in green.

fitting of our model onto the latter. Starting values for this fitting are provided in table 8 in the SI. The light blue line in figure 6(a) again shows the fit of our model onto the data points of emission R_{20}. It clearly follows the trends among the data points and the obtained fitting parameters, appended to table 8 in the SI, are reasonably close to their starting values. The dashed dark red line, as based on inserting the obtained fitting parameters into the rate equation solution for N_1, is not able to perfectly mirror the measured intensity trends in emission R_{10}. Especially at temperatures below 100 K, where 4f–4f emission R_{10} is measured but not simulated by our model, and above 200 K, where the measured intensity is much lower than predicted.

From figure 6(c), it follows that for $CaI_2:Tm^{2+}$ the quenching of emission R_{20} is too strong for performing a fitting analysis with our model. Panel d shows that this is due to a large value of W_{21} compared to W_{32} as explained at the end of section 3.3.

The obtained steady-state fitting parameters for $CaBr_2:Tm^{2+}$ and $CaCl_2:Tm^{2+}$, allow it to plot the non-radiative rate W_{21} over temperature and inspect the development of the MPR and IC processes. Figure 7 shows these plots with colour coding in analogy to figure 5. For both materials the low temperature region is governed by MPR, while at high temperatures IC is dominant in $CaCl_2:Tm^{2+}$ (panel a). In case of $CaBr_2:Tm^{2+}$ (panel b), the MPR process stays strongest at even high temperatures; which differs from figure 7. Nevertheless both processes seems clearly involved in the quenching. For $CaBr_2:Tm^{2+}$, the non-radiative rate W_{21} outmatches the radiative rate R_{20} at around 160 K and the quenching prevails. For $CaCl_2:Tm^{2+}$ this seems to happen at a slightly higher temperature.

3.5. *Model limitations*

The quenching of 5d–4f emission R_{20} and intensification of 4f–4f emission R_{10} predicts the presence of a risetime phenomena in the luminescence lifetime curves of the latter. Such a phenomena has been observed several times before in similar materials [8, 22]. The solid curves in figure 8 reveal that also for $CaBr_2:Tm^{2+}$ a risetime is measured, even at 20 K. The curves predicted by our three-level combined quenching model (MPR + IC), using fitting parameters from table 3 column 3, are provided by the dashed curves. For temperatures above 200 K, the curves overlap well with the experimental data. At lower temperatures however, where the 4f–4f emission intensity is very weak, the risetime predicted by the model is longer than experimentally measured. This discrepancy arises from a limitation of our model that is discussed in the next subsection.

3.5.1. HS → LS Interaction and 4-level model. So far we have assumed that the population of the 5d ($^3H_6$,t_{2g}) LS state, immediately after excitation, is lost to the lower lying 5d (3H_6,t_{2g}) HS state at all temperatures. It has allowed us to describe the feeding of 4f–4f luminescence by the 5d manifold and assign a combination of multi-phonon relaxation and interband cross-

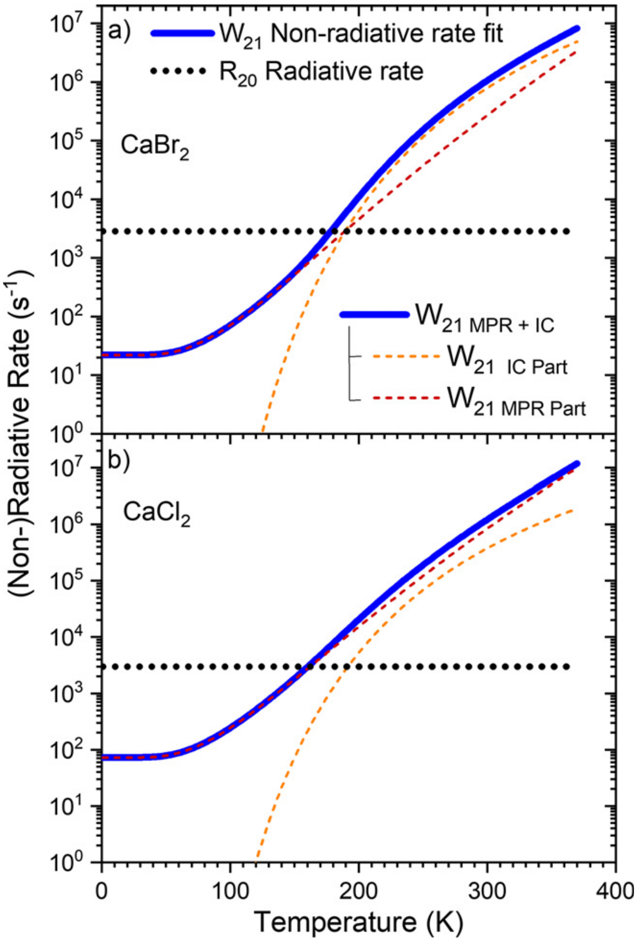

Figure 7. The obtained W_{21} parameters of (a) $CaCl_2:Tm^{2+}$ and (b) $CaBr_2:Tm^{2+}$ plotted in blue and versus temperature. The dark red and orange dashed lines respectively reveal the MPR and IC constituents, while the dotted black line shows the R_{20} radiative rate.

ing to such a temperature quenching process. However, it has been observed in various halides [5, 29] that at low temperatures the LS-state population is significant and actually also the required time and/or temperature for LS → HS depopulation cannot be neglected. Here we present some evidence for LS → HS states interaction and discuss its influence on our model.

In figure 9 the lifetimes of the 5d–4f ($3H_6$,t_{2g}) HS emission (blue dots) are compared to the risetimes of the 4f–4f emission (red dots) for $CaX_2:Tm^{2+}$ ($X = $ Cl, Br, I). Both emissions are monitored after excitation into the 5d ($3H_6$,t_{2g}) LS levels. The ($3H_6$,t_{2g}) HS lifetimes were obtained via a single exponential fitting of the 5d–4f decay curves, whereas a similar fitting strategy on 0–1 ms timescale was used for retrieving the 4f–4f risetimes. As is observed the lifetime of the ($3H_6$,t_{2g}) HS emission behaves in a simple manner: at 20 K the lifetime τ_d amounts to ~300 μs (~30 μs for $CaI_2:Tm^{2+}$) and as the temperature increases it becomes shorter due to thermal quenching. This is well in-line with the measurements and modelling of its emission behaviour, see for instance figure 6. As discussed in previous sections, the quenching is due to a non-radiative feeding of 4f $^2F_{5/2}$ level. As such, it is expected that the time scale related to the decay of the 5d–4f HS emission is reflected in the risetime components of the 4f-4f $^2F_{5/2} \rightarrow {}^2F_{7/2}$ emission. In case of $CaI_2:Tm^{2+}$ this is observed at all temperatures. For $CaCl_2:Tm^{2+}$ and $CaBr_2:Tm^{2+}$ the risetime τ_r components of the 4f–4f emission (red) are in good agreement with the 5d–4f HS lifetimes τ_d (blue) only above ~150 K. Below 150 K the 4f–4f risetimes deviate strongly from the 5d–4f HS lifetimes. While the 5d–4f HS lifetimes are around ~300 μs, the τ_r rise-times behave in a non-monotonic manner: for example in $CaBr_2:Tm^{2+}$ at 20–50 K τ_r is relatively short, in the order of a few microseconds; whereas between 50–150 K it increases up to ~100 μs. This behaviour of the 4f–4f emission risetimes has been reported for $CsCaX_3:Tm^{2+}$ [30] and is connected to the non-radiative relaxation from an LS to HS 5d-state during the feeding of a 4f excited state. Applied to our case, the short risetimes at 10–50 K could then be due to an LS 5d → 4f non-radiative relaxation with strong electron-phonon coupling. The 50–150 K increase in τ_r is due to LS → HS thermally activated relaxation: partially populated HS and LS 5d-states both feed the $^2F_{5/2}$ state.

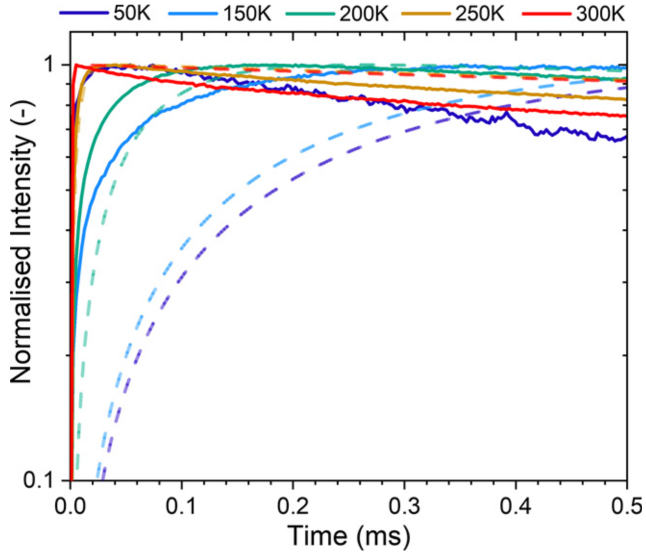

Figure 8. Normalised luminescence lifetime curves of 4f–4f emission R_{10} plotted at various temperatures, clearly displaying a risetime phenomenon. The solid curves represent experimental data, whereas the dashed transparent curves are plots based on our combined quenching model.

The existence of 4f–4f emission after excitation into 5d manifold already at 10 K points to multi-phonon channel as the only relaxation process not disabled at He-temperatures [24, 28]. In various compounds, the onset of LS → HS non-radiative relaxation is related to the energy difference between LS and HS states, the optical phonon mode to which the relaxation couples and the phonon coupling strength [24, 26, 28]. For the former two parameters (host phonon modes, $h\omega_{LO}$, and LS-HS energy separation, $E_{HS\text{-}LS}$) the values can be obtained from literature. We have decided to check the relation between LS-HS populations with risetime behaviour for various compounds known from literature. Figure 6 in the SI reveals that there is a trend between the energy difference between the LS

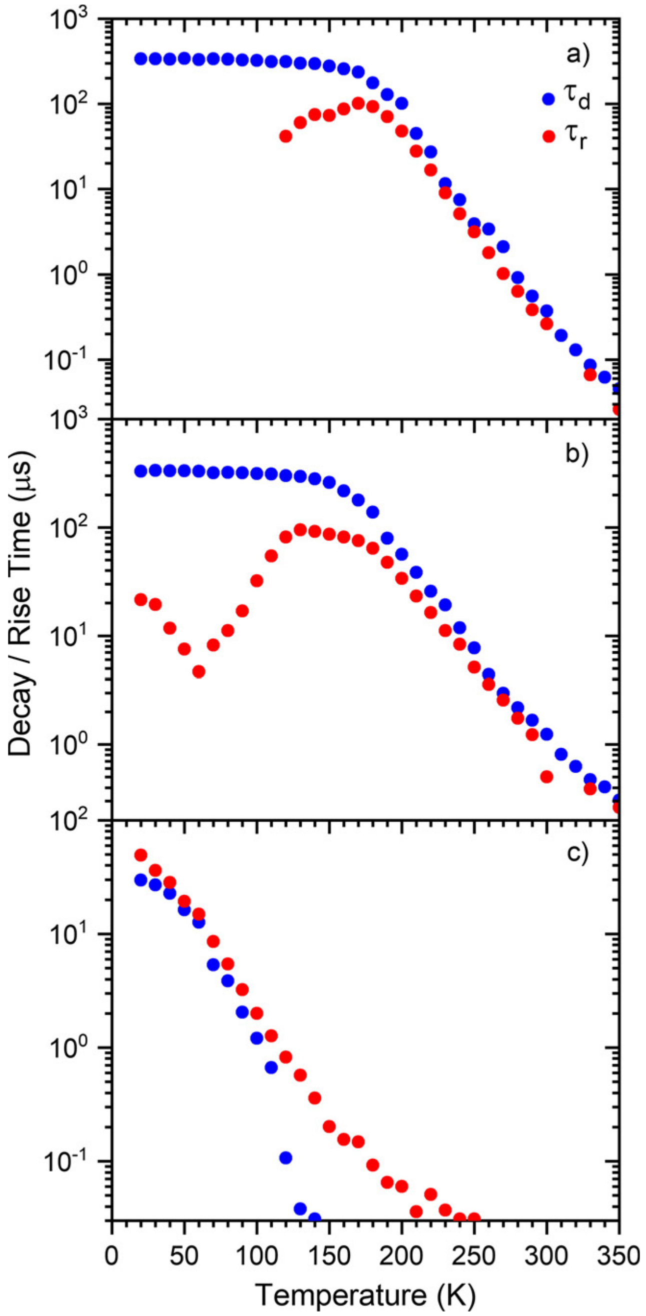

Figure 9. Temperature dependence of the lifetime (τ_d) related to the 5d–4f ($^3H_6$,t_{2g}) HS emission and risetime (τ_r) of the 4f–4f emission in: (a) $CaCl_2$:Tm^{2+}, (b) $CaBr_2$:Tm^{2+} and (c) CaI_2:Tm^{2+}. The emissions were monitored after excitation into the ($^3H_6$,t_{2g}) LS levels.

and HS states, in number of required phonons, and the T_{50} temperature quenching onset related to the 5d LS-depopulation. The dependence has a huge uncertainty and deviation due to unknown phonon coupling strengths, but still we can expect that in our $CaCl_2$:Tm^{2+} and $CaBr_2$:Tm^{2+} compounds the LS 5d-state actively loses population at around 100–150 K, which is consistent with the observations in risetime kinetics in figure 9.

In the new assumption that below 150 K the electrons in the 5d ($^3H_6$,t_{2g}) LS state do not immediately thermally relax to the HS state, we need to consider a 4-level system for our modelling.

3.5.2. Possible mechanisms for confined QE. Direct QE measurements with an integrating sphere have resulted in QE-values that are considerably lower than the 100% predicted by our model. Our data does not hint at any process explaining the lower-than-expected QE values. Below we suggest four possibilities that still need to be confirmed experimentally in future work. It may be that the QE-measurements are inaccurate. The special sample holder in the integrating sphere, that protects the powder sample from hygroscopicity and oxidation, may absorb part of the Tm^{2+} NIR luminescence despite the fact it is made from Teflon and quartz parts. Alternatively, our samples may partly absorb excitation light by impurities or defects other than the Tm^{2+} ions, this despite our approach to measure the absorption relative to undoped samples when calculating QE-values. In terms of luminescence quenching mechanisms, the lower QE-values may be caused by a thermally stimulated electron delocalisation to the conduction band as was explained our work on NaX:Tm^{2+} mono-halides [8]. Our unpublished low temperature excitation and emission measurements on Tm^{3+}-doped CaX_2 (X = Cl, Br, I) has revealed clear features related to bandgaps and CT bands. It does however not allow us to determine the energy of the lowest 5d-state with respect to the conduction band bottom with high enough certainty to decide on the possibility of this process. Finally, concentration quenching from the excited 4f- or 5d-states can result in a lower QE. In SrI_2:Tm^{2+} [23] concentration quenching only starts above 3 mol % Tm^{2+}-doping. In other hosts like NaI [39] the quenching starts at a somewhat lower doping percentage of 0.5 mol %. With a Tm^{2+} concentration of about 1 mol % in our samples, there may be some quenching but from the observed decay times of the 4f–4f emission of 3.6–5.3 ms it is likely not a strong process.

4. Conclusions

The excited states dynamics of Tm^{2+} as doped in CaX_2 (X = Cl, Br, I) were investigated. At 20 K up to four distinct Tm^{2+} emissions were observed, corresponding to the transitions: ($^3F_4$,t_{2g}) → $^2F_{7/2}$, ($^3H_6$,t_{2g})$_{S=1/2}$ → $^2F_{7/2}$, ($^3H_6$,t_{2g})$_{S=3/2}$ → $^2F_{7/2}$ and $^2F_{5/2}$ → $^2F_{7/2}$. As the temperature increases to 100 K the ($^3F_4$,t_{2g}) → $^2F_{7/2}$ and ($^3H_6$,t_{2g})$_{S=1/2}$ → $^2F_{7/2}$ 5d–4f emissions undergo quenching via 5d–5d multi-phonon relaxation and only the lowest-energy ($^3H_6$,t_{2g})$_{S=3/2}$ → $^2F_{7/2}$ 5d–4f emission and the $^2F_{5/2}$ → $^2F_{7/2}$ 4f–4f emission remain. A rate equation model was developed to describe the subsequent non-radiative feeding from the ($^3H_6$,t_{2g})$_{S=3/2}$ 5d-state towards the $^2F_{5/2}$ 4f-state. The model was successfully fitted onto the temperature- and time-dependent luminescence intensity data of $CaBr_2$:Tm^{2+} and $CaCl_2$:Tm^{2+}, where it is revealed that the non-radiative relaxation occurs via two different processes. At low temperatures multi-phonon relaxation towards the $^2F_{5/2}$-level dominates, which explains the presence of the $^2F_{5/2}$ → $^2F_{7/2}$ emission at 20 K. As the temperature increases, to typically 130 K, the additional process of interband crossing is thermally activated. As a result only the $^2F_{5/2} \rightarrow {}^2F_{7/2}$ emission is observed at room temperature.

Although the quantitative fitting approach describes the overall temperature- and time-dependent well, two interesting deviations were observed and discussed. Firstly, at low temperature, we observe a risetime for the $^2F_{5/2} \rightarrow {}^2F_{7/2}$ emission, 15 times shorter than predicted by the model; which can likely be explained by an LS → HS resonance energy transfer interaction between neighboring Tm^{2+} ions. Secondly, we observe a $^2F_{5/2} \rightarrow {}^2F_{7/2}$ quantum efficiency of 20–30% after $^2F_{7/2} \rightarrow (^3H_6,t_{2g})_{S=1/2}$ excitation for all three dihalides. Our model predicts a QE of 100% as it does not contain a non-radiative process to the ground state. Different explanations for this were provided and discussed, such as: absorption of $^2F_{5/2} \rightarrow {}^2F_{7/2}$ emission light by the hygroscopic sampleholder, partial excitation light absorption by impurities and defects, a thermally stimulated electron delocalization route to the conduction band, and concentration quenching effects.

This study allow us to gain a better understanding of the quenching processes of the Tm^{2+} excited 5d-manifold and related feeding of the $^2F_{5/2} \rightarrow {}^2F_{7/2}$ emission. Based on the variety in phonon energies, 5d-level positions and Stokes' shifts of CaX_2:Tm^{2+} (X = Cl, Br, I), we were able to significantly shift the temperature onset of these processes. It provides design criteria for stable Tm^{2+} $^2F_{5/2} \rightarrow {}^2F_{7/2}$ luminescence to be used for photovoltaic energy conversion in LSCs.

Acknowledgments

This research was financially supported by the Nederlandse Organisatie voor Wetenschappelijk onderzoek (NWO) as part of the LumiCon Project 15024 proposal. The authors would like to thank JTM. de Haas (TU Delft) for overall support with the photoluminescence setups and RD Abellon (TU Delft) and BE Terpstra for experimental support with respectively the fluorescence quantum yield measurements and ICP-OES experiments.

Data availability statement

The data that support the findings of this study are available upon reasonable request from the authors.

ORCID iDs

M P Plokker https://orcid.org/0000-0002-1939-0649

References

[1] Debije M G and Verbunt P P C 2012 Solar concentrators: thirty years of luminescent solar concentrator research: solar energy for the built environment *Adv. Energy Mater.* **2** 12–35

[2] Meinardi F, Bruni F and Brovelli S 2017 Luminescent solar concentrators for building-integrated photovoltaics *Nat. Rev. Mater* **2** 17072

[3] ten Kate O M, Krämer K W and Van der Kolk E 2015 Efficient luminescent solar concentrators based on self-absorption free, Tm2+ doped halides *Sol. Energy Mater. Sol. Cells* **140** 115–20

[4] Grimm J and Güdel H U 2005 Five different types of spontaneous emission simultaneously observed in Tm^{2+} doped $CsCaBr_3$ *Chem. Phys. Lett.* **404** 40–3

[5] Grimm J, Suyver J F, Beurer E, Carver G and Güdel H U 2006 Light-emission and excited-state dynamics in Tm^{2+} doped $CsCaCl_3$, $CsCaBr_3$, and $CsCaI_3$ *J. Phys. Chem.* B **110** 2093–101

[6] Beurer E, Grimm J, Gerner P and Güdel H U 2006 Absorption, light emission, and upconversion properties of Tm^{2+}-doped $CsCaI_3$ and $RbCaI_3$ *Inorg. Chem.* **45** 9901–6

[7] Grimm J, Wenger O S, Krämer K W and Güdel H U 2006 4f–4f and 4f–5d excited states and luminescence properties of Tm^{2+}-doped CaF_2, $CaCl_2$, $SrCl_2$, $BaCl_2$ *J. Phys. Chem* B **110** 101–5

[8] Plokker M P and van der Kolk E 2019 Temperature dependent relaxation dynamics of luminescent NaX: Tm^{2+} (X = Cl, Br, I) *J. Lumin.* **216** 116694

[9] Karbowiak M and Rudowicz C 2018 Trends in Hamiltonian parameters determined by systematic analysis of f–d absorption spectra of divalent lanthanides in alkali-halides hosts: II. $CaCl_2$:Ln^{2+} (Ln = Sm, Eu, Tm, and Yb) *J. Lumin.* **197** 66–75

[10] Raptis C, Krobok M and Holzapfel W B 1992 Pressure dependence of Raman-active phonons of $CaBr_2$ *High Press. Res.* **9** 27–30

[11] Baskurt M, Yagmurcukardes M, Peeters F M and Sahin H 2020 Stable single-layers of calcium halides (CaX_2, X = F, Cl, Br, I) *J. Chem. Phys.* **152** 164105

[12] ten Kate O M, Zhang Z, Dorenbos P, Hintzen H T and van der Kolk E 2013 4f and 5d energy levels of the divalent and trivalent lanthanide ions in $M_2Si_5N_8$ (M = Ca, Sr, Ba) *J. Solid State Chem.* **197** 209

[13] Rogers E, Dorenbos P, de Haas J T M and van der Kolk E 2012 Experimental study of the $4f^n \rightarrow 4f^n$ and $4f^n \rightarrow 4f^{n-1}\ 5d^1$ transitions of the lanthanide diiodides LnI_2 (Ln = Nd, Sm, Eu, Dy, Tm, Yb) *J. Phys.: Condens. Matter.* **24** 275502

[14] Dieke G H and Crosswhite H M 1963 The spectra of the doubly and triply ionized rare earths *Appl. Opt.* **2** 675–86

[15] Dorenbos P 2003 Energy of the first $4f^7 \rightarrow 4f^6 5d$ transition of Eu^{2+} in inorganic compounds *J. Lumin.* **104** 239–60

[16] Larsen P P 2004 Lumineszenz zweiwertiger selten-erd-ionen in bromidischen wirtsgittern *PhD Thesis* Universität zu Köln

[17] Lehmann W 1975 Heterogeneous halide-silica phosphors *J. Electrochem. Soc.* **122** 748

[18] Gahane D H, Kokode N S, Muthal P L, Dhopte S M and Moharil S V 2009 Luminescence of Eu^{2+} in some iodides *Opt. Mater.* **32** 18–21

[19] de Jong M, Meijerink A, Seijo L and Barandiarán Z 2017 Energy level structure and multiple $4f^{12}5d^1$ emission bands for Tm^{2+} in halide perovskites: theory and experiment *J. Phys. Chem.* C **121** 10095–101

[20] van Aarle C, Dorenbos P and Kraemer K W 2021 The role of Yb^{2+} as a scintillation sensitiser in the near-infrared scintillator $CsBa_2I_5$:Sm^{2+} *J. Lumin.* (in review)

[21] Blasse G and Grabmeier B C 1994 *Luminescent Materials* (Berlin: Springer)

[22] Struck C W and Fonger W H 1991 *Understanding Luminescence Spectra and Efficiency Using* W_p *and Related Functions* (*Inorganic Chemistry Concepts 13*) (Berlin: Springer)

[23] Plokker M P, Hoogsteen W, Abellon R D, Krämer K W and van der Kolk E 2020 Concentration and temperature dependent luminescence properties of the SrI_2-TmI_2 system *J. Lumin.* **225** 117327

[24] Reisfeld R and Jörgensen C K 1977 *Lasers and Excited States of Rare-Earths* (*Inorganic Chemistry Concepts 1*) (Berlin: Springer)

[25] Yu D, Ballato J and Riman R E 2016 Temperature-dependence of multiphonon relaxation of rare-earth ions in solid-state hosts *J. Phys. Chem* C **120** 9958–64

[26] Tanabe S, Yoshii S, Hirao K and Soga N 1992 Upconversion properties, multiphonon relaxation, and local environment of rare-earth ions in fluorophosphate glasses *Phys. Rev.* B **45** 4620

[27] Yen W M, Shionoya S and Yamamoto H 2007 *Phosphor Handbook* 2nd edn (Boca Raton: CRC Press, Taylor & Francis Group) ch 2

[28] Di Bartolo B 1991 *Advances in Nonradiative Processes in Solids* (*NATO Advanced Science Institutes Series, Series B. Physics V. 249*) (Berlin: Springer)

[29] Suta M and Wickleder C 2017 Spin crossover of Yb^{2+} in $CsCaX_3$ and $CsSrX_3$ (X = Cl, Br, I)—a guideline to novel halide-based scintillators *Adv. Funct. Mater.* **27** 1602783

[30] Koster S, Reid M, Wells J P and Reeves R 2014 Energy levels and dynamics of Tm^{2+} doped into AMX3 salts *Msc Thesis* University of CanterburyS. Koster

[31] Uriarte L M, Dubessy J, Boulet P, Baonza V G, Bihannic I and Robert P 2015 Reference Raman spectra of synthesized $CaCl_2 \cdot nH_2O$ solids ($n = 0, 2, 4, 6$) *J. Raman Spectrosc.* **46** 10

[32] Cui Y *et al* 2011 Raman spectroscopy study of Bai_2:Eu and SrI_2:Eu scintillator crystals *Solid State Commun.* **151** 7

[33] Tsuboi T, Witzke H and McClure D S 1981 The $4f^{14} \rightarrow 4f^{13}5d$ transition of Yb^{2+} ion in NaCl crystals *J. Lumin.* **24–25** 305–8

[34] Alekhin M S, Biner D A, Krämer K W and Dorenbos P 2014 Optical and scintillation properties of SrI2:Yb^{2+} *Opt. Mater.* **37** 382–6

[35] Hendriks M and van der Kolk E 2019 4f → 5d and anomalous emission in Yb^{2+} doped NaI, SrI_2 and LaI_3 powders prepared by rapid melting and quenching in vacuum *J. Lumin.* **207** 231–5

[36] Pan Z, Duan C K and Tanner P A 2008 Electronic spectra and crystal field analysis of Yb^{2+} in $SrCl_2$ *Phys. Rev.* B **77** 085114

[37] Burstein E, Johnson F A and Loudon R 1965 Selection rules for second-order infrared and Raman processes in the rocksalt structure and interpretation of the Raman spectra of NaCl, KBr, and NaI *Phys. Rev.* **139** A1239

[38] Schreyer D, Waschk V and Châtelain A 1981 Raman spectroscopy in small crystals of $SrCl_2$ *Surf. Sci.* **106** 336–44

[39] Merkx E P J, Plokker M P and van der Kolk E 2021 The potential of transparent sputtered NaI:Tm^{2+}, CaBr2:Tm^{2+}, and CaI_2:Tm^{2+} thin films as luminescent solar concentrators *Sol. Energy Mater. Sol. Cells* **223** 110944